CHALMERS
UNIVERSITY OF TECHNOLOGY

Probing resistive switching in HfO<inf>2</inf>/Al<inf>2</inf>O<inf>3</inf> bilayer oxides using in-situ

Downloaded from: https://research.chalmers.se, 2026-04-04 16:53 UTC

Citation for the original published paper (version of record):

Ranjan, A., Xu, H., Wang, C. et al (2023). Probing resistive switching in HfO<inf>2</inf>/Al<inf>2</inf>O<inf>3</inf> bilayer oxides using in-situ transmission electron microscopy. Applied Materials Today, 31.
http://dx.doi.org/10.1016/j.apmt.2023.101739

N.B. When citing this work, cite the original published paper.

research.chalmers.se offers the possibility of retrieving research publications produced at Chalmers University of Technology. It covers all kind of research output: articles, dissertations, conference papers, reports etc. since 2004. research.chalmers.se is administrated and maintained by Chalmers Library

(article starts on next page)

Applied Materials Today 31 (2023) 101739

Contents lists available at ScienceDirect

Applied Materials Today

journal homepage: www.elsevier.com/locate/apmt

Probing resistive switching in HfO_2/Al_2O_3 bilayer oxides using *in-situ* transmission electron microscopy

Alok Ranjan [a,b,1,*], Hejun Xu [c,1], Chaolun Wang [c,1], Joel Molina [d], Xing Wu [c,*], Hui Zhang [e], Litao Sun [e], Junhao Chu [f], Kin Leong Pey [a,*]

[a] Engineering Product Development Pillar, Singapore University of Technology and Design, 8 Somapah Road, 487 372, Singapore
[b] Department of Physics, Chalmers University of Technology, Gothenburg, 412 96, Sweden
[c] School of Communication and Electronic Engineering, East China Normal University, 500 Dongchuan Road, Shanghai, 200 241, China
[d] Department of Electronics, National Institute of Astrophysics, Optics and Electronics, Tonantzintla, Puebla, 72 840, Mexico
[e] SEU-FEI Nano-Pico Center, Key Laboratory of MEMS of Ministry of Education, Collaborative Innovation Center for Micro/Nano Fabrication, Device and System, Southeast University, Nanjing, 210096, China
[f] School of Physics and Electronic Science, East China Normal University, 500 Dongchuan Road, Shanghai, 200 241, China

ARTICLE INFO

Keywords:
Diffusion Barrier
Metal migration
Reliability
Resistive Memory
TEM

ABSTRACT

In this work, we investigate the resistive switching in hafnium dioxide (HfO_2) and aluminum oxide (Al_2O_3) bilayered stacks using *in-situ* transmission electron microscopy and X-ray energy dispersive spectroscopy. Conductance of the HfO_2/Al_2O_3 stack changes gradually upon electrical stressing which is related to the formation of extended nanoscale physical defects at the HfO_2/Al_2O_3 interface and the migration and re-crystallization of Al into the oxide bulk. The results suggest two competing physical mechanisms including the redistribution of oxygen ions and the migration of Al species from the Al electrode during the switching process. While the HfO_2/Al_2O_3 bilayered stack appears to be a good candidate for RRAM technology, the low diffusion barrier of the active Al electrode causes severe Al migration in the bi-layered oxides leading to the device to fail in resetting, and thereby, largely limiting the overall switching performance and material reliability.

1. Introduction

As Flash technology for data storage is reaching its scaling limits, multiple high value alternative non-volatile memory (NVM) technologies have been identified over the years [1]. Resistive random-access memory (RRAM) is one such alternate NVM technology that has attracted enormous interests as it meets the requirements of emerging data centric engineering (e.g., neuromorphic, and deep learning edge computations) and low power (e.g., healthcare, internet of things (IoT), sensors and wearables) applications of the 21st century [2–4]. This is due to its demonstrated high switching speeds (~pico-seconds) [5–7], ultra-low switching energy (~pico-joules) [8–10], small device footprint ($<10\times10$ nm^2) [11], digital and analog switching [12,13], multi-bit data storage capability [14] and ease of integration with the CMOS process flow [15,16].

RRAM in its simplest form consists of a metal-insulator-metal (MIM) stack in which the toggling between the two stable resistance states is achieved by current/voltage-controlled nucleation and rupture of nanoscale conductive filaments (CFs) [17]. A CF can comprise a high concentration of metal ions/atoms, accumulated oxygen vacancies (V_O), or a mix of the two depending on the choice of oxide and electrode materials and electrical switching conditions, e.g., current compliance [17,18]. A wide pool of dielectrics/oxides and metal electrodes combinations have demonstrated resistive switching. However, many reliability challenges including device-to-device and cycle-to-cycle variability, endurance, and retention issues have limited its practical applications. Research efforts, therefore, have been directed towards multiple-objective optimization of the RRAM material stack considering the four major reliability criteria: endurance, retention, radiation, and read-disturb noise and three major performance criteria: low power, large memory window and low filament forming voltage, all at once [19–22]. Very recently, RRAM has been successfully demonstrated at

* Corresponding authors.
E-mail addresses: alok.ranjan@chalmers.se (A. Ranjan), xwu@cee.ecnu.edu.cn (X. Wu), peykinleong@sutd.edu.sg (K.L. Pey).
[1] Equal contributions.

https://doi.org/10.1016/j.apmt.2023.101739
Received 25 September 2022; Received in revised form 24 December 2022; Accepted 16 January 2023
Available online 19 January 2023
2352-9407/© 2023 The Author(s). Published by Elsevier Ltd. This is an open access article under the CC BY license (http://creativecommons.org/licenses/by/4.0/).

the production level in a 28 nm process technology on 300 mm wafers and volume production is expected soon [23].

HfO_2/Al_2O_3 bi-layer stacks is being considered as a potential material system of interest for many applications including sensors, photoactive technology (solar cell, passivation, and absorption layers), nanostructured thin films (quantum well formation and refractive coatings), quantum bit technology and a switching material for RRAM technology [11,24-26]. Recent works have demonstrated that HfO_2/Al_2O_3-based bilayered RRAM [27,28] stacks improve overall endurance and reliability [29–35], as Al_2O_3 layer hinders the diffusion of oxygen ions and acts as a diffusion barrier. This allows HfO_2/Al_2O_3 based RRAM stacks to realize multilevel resistance states [36] which have applications in emerging neuromorphic computing. However, there is limited experimental evidence in understanding the underlying physical and chemical changes occurring in bilayer HfO_2/Al_2O_3 RRAM stacks during resistive switching events [28] and the migration of related atomic species during RRAM operation and its impact on switching performance are still open questions.

In this context, transmission electron microscopy (TEM) and related spectroscopy techniques have emerged as a powerful tool to observe the atomic scale phenomena in wide range of applications. Numerous previous studies were carried out in gate dielectrics (e.g., SiO_2, SiO_xN_y and HfO_2) to understand degradation and electrical breakdown using TEM techniques [37,38]. Given that the underlying physics governing the dielectric breakdown and the formation of conduction filament in RRAM are similar, many insights can be drawn from these previous studies. While most of the prior works on RRAM and gate dielectrics have been undertaken using *ex-situ* TEM approach (i.e., the device is stressed first outside the TEM and then investigated in TEM), recent developments in the *in-situ* electrical stressing TEM holders allow to observe the physical phenomenon in real-time. Some of the notable previous *in-situ* TEM works have investigated the resistive switching mechanism in HfO_2 [39], TiO_2 [40] and Ta_2O_{5-x}/TaO_{2-x} [41] based RRAM devices. Specifically, these studies have provided insights into many aspects of the resistive switching including: (a) the composition of CF(s) formed under different electrical polarities for various RRAM stacks [39], (b) the correlation of CF(s) size/dimensions with current compliance used [42,43], (c) existence of multiple correlated and uncorrelated CFs [44] and (d) the role of oxide-electrode interface in switching [45].

Therefore, in this work, we have specifically designed, and fabricated HfO_2/Al_2O_3-based bilayered RRAM devices with W and Al as working electrodes. The measurements have been done *in-situ* using a TEM and custom-designed nano-pillar test structure [43]. The choice for electrodes have been carefully made so as to investigate the switching mechanism depending on both current compliance and electrical polarities. Our experimental approach allows to systematically create, confine, and investigate the physical and chemical changes at multiple nanoscale CFs in the same TEM specimen during a single experiment. We find that the conductance of the HfO_2/Al_2O_3 based RRAM changes gradually and is related to the migration and crystallization of Al from the Al electrode into the oxide bulk. The formation of nanoscale physical defect at the HfO_2/Al_2O_3 interface is observed during electrical stressing. The results suggest the existence of two competing switching mechanisms including the redistribution of oxygen ions and the migration of Al. These findings would be useful in the optimization of RRAM stacks for improving performance and reliability of HfO_2/Al_2O_3-based RRAM stacks.

2. Experimental

2.1. Device fabrication

A n^{++} type Si wafer (100) (resistivity (ρ) < 0.005 Ω cm) is used as substrate. Si substrate is pre-cleaned by sequential immersion in trichloroethylene (TCE) and acetone within an ultrasonic vibrator in order to remove the organic contaminants. Standard Radio Corporation of America (RCA) cleaning is used to remove both organic and ionic contaminants. Finally, the substrate is cleaned in a HF solution to remove native oxide. An Al film of ~5 μm thickness is then deposited using e-beam evaporator (Temescal, BJD-1800™) in a high vacuum condition (working pressure of 10^{-6} Torr) at a rate of ~1 nm/s. The rate of the metal deposition has been optimized to obtain denser Al films, since using slower deposition rates for this metal would prevent proper nucleation (see Supplementary Figure 1). A 4 nm Al_2O_3 and 4 nm HfO_2 film were then sequentially deposited using atomic layer deposition (ALD) (Savannah-S100, Cambridge-Nanotech™) using H_2O, TMA and TDMAH as precursor gasses at a temperature of 250 °C. Finally, a 250 nm thick W top electrode is deposited at the rate of 0.2 nm/s using the same e-beam evaporator (working pressure of 10^{-5} Torr) to obtain $W/HfO_2/Al_2O_3/Al$ RRAM device.

2.2. TEM sample preparation

2 μm Pt is deposited on $W/HfO_2/Al_2O_3/Al$. The sacrificial Pt metallic protection layer is purposely chosen as it will also serve as top electrical contact during the *in-situ* electrical measurements. Approximately 12 μm long and 60 nm wide TEM lamella is prepared using a focused gallium ion beam in a FEI dual-beam Helios™ 600i system. FIB milling is further carried out to create isolated nano-pillars of length 500 nm, which acts as individual RRAM nano-device. A single FIB lamella contains 10 individual RRAM devices which greatly improves the efficiency of the *in-situ* measurements. As prepared FIB lamella is attached on a conductive half Cu TEM grid and is used for the *in-situ* TEM measurements. Finally, a low energy (3 keV) ion milling is applied to remove the residues and surface contaminants from the prepared TEM specimen.

2.3. Ex-situ TEM

The structural analysis of the as-prepared RRAM nano-devices is carried out using a 300 kV operated image aberration-corrected TEM (JEM-ARM300F™). X-ray electron energy dispersive x-ray (XEDX) is used for the elemental analysis.

2.4. In-situ TEM

A probe aberration-corrected TEM (FEI Titan™) with a 200 kV accelerating voltage is used for all the *in-situ* imaging and electrical spectroscopy measurements. The electron beam is carefully spread out during the measurements to avoid e-beam induced damages while maintaining a relatively high atomic resolution. The *in-situ* measurements have been performed in a dedicated STM-TEM holder (Nanofactory Instruments AB™). The holder allows to precisely bring a nanometallic tip in direct physical contact with the individual nano-pillar RRAM device and apply electrical stress with current compliance in place.

3. Results and discussion

3.1. Device fabrication and test methodology

The device used in this study consists of an asymmetric MIM structure: Tungsten (W) as the top electrode, HfO_2 (4 nm) and Al_2O_3 (4 nm) as dielectric layers and Aluminum (Al) as the bottom electrode. HfO_2 and Al_2O_3 films were deposited at 250 °C using atomic layer deposition (ALD), and the metal electrodes (W and Al) are deposited using e-beam evaporation as discussed in Section 2. The e-beam evaporation is preferentially used here for the electrode deposition to achieve a higher control in the deposition rate and avoid plasma related damages as commonly observed in the metal films deposited by sputtering techniques (see Supplementary Note 1 for discussions). We purposely used asymmetric electrodes consisting of W and Al primarily due to their different chemical diffusivity, ion mobility and oxygen scavenging

properties. While, Al has higher diffusivity and ionic mobility in high-κ dielectrics [46], W is typically employed for low power oxygen vacancy-based RRAM devices [10,47]. Therefore, in principle, a $W/HfO_2/Al_2O_3/Al$ based asymmetric MIM structure can be used to create "oxygen vacancy" or "metallic" conduction filament depending on the voltage polarities and current compliance used.

Sacrificial Pt layer is deposited on $W/HfO_2/Al_2O_3/Al$ and a dual beam focused ion beam (FIB) milling is used to create nano-pillar RRAM devices as shown schematically in Fig. 1a. This approach allows to create multiple RRAM devices on a single FIB lamella. The devices are both physically and electrically isolated and this allows to test each of the device under various electrical stress (polarity, current compliance etc.) conditions. This significantly reduces the FIB sample preparation time that would be needed to create individual TEM specimens for the *in-situ* measurements. Each RRAM device is approximately 500 nm in length and 60 nm in width (i.e., electron transparent in the TEM observation directions) and physically separated from each-other by 500 nm as shown in Fig. 1b. During the sample fabrication, we purposely use a thicker bottom Al electrode ($\sim 5\ \mu m$), as this allows to keep the multiple nano-devices electrically connected to the global Al bottom electrode while physically separating each of the individual RRAM nano-devices.

A bright field high resolution TEM (HRTEM) micrograph of one of the as prepared nano-device is shown in Fig. 1c. Al_2O_3 and HfO_2 switching oxide films are amorphous and form sharp interfaces with oxide and metal electrode layers. This is expected as ALD is known to create films with homogeneous thickness allowing us to decouple the

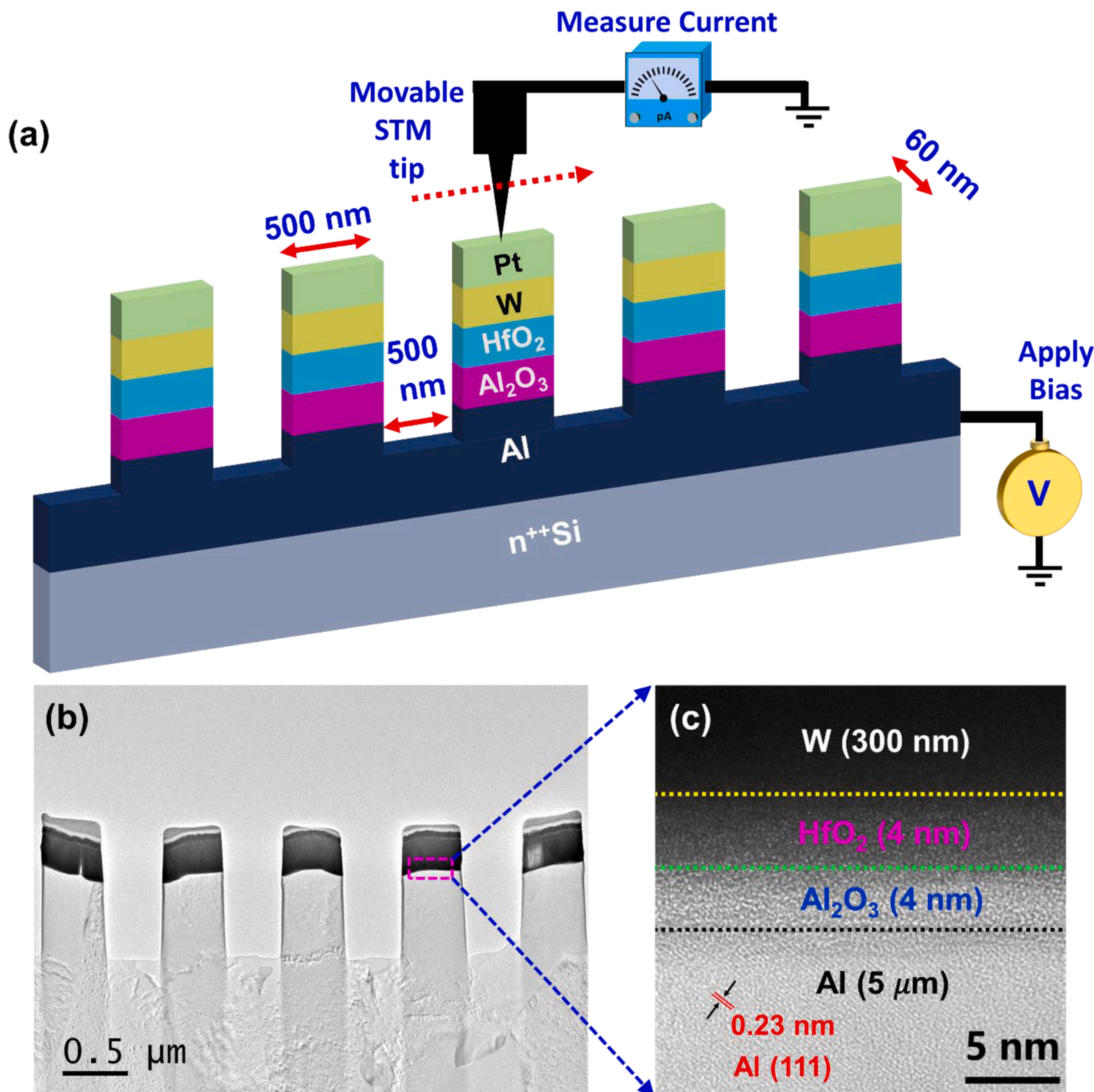

Fig. 1. a) Schematic showing the TEM specimen containing multiple physically and electrically isolated nano-pillar RRAM devices and experimental set-up for *in-situ* electrical characterization. Each individual pillar consists of identical MIM stack of W (top, 300 nm)/HfO_2 (4 nm)/Al_2O_3 (4 nm)/Al (bottom, 5 μm). The TEM specimen is mounted on a half copper TEM grid and a tungsten STM tip is used to make physical contact to the top electrode Pt using a dedicated *in-situ* STM-TEM electrical stressing holder. During the electrical measurements, a bias is always applied to the bottom electrode and the STM tip is electrically grounded. b) Low resolution TEM micrograph showing the overview of the TEM specimen prepared. A sacrificial Pt film is deposited during the FIB ion milling. c) High resolution TEM (HRTEM) micrograph of one of the RRAM nano-device showing the switching oxide layers, and metal electrodes.

role of local oxide thickness variations in the resistive switching process. We also note that while the as-deposited W is amorphous, Al film is crystalline as evident from the lattice fringes observed in Fig. 1c. Analysis shows that the lattice constant for the observed fringes is 0.23 nm which corresponds to Al (111) crystal plane [48].

The experimental set-up for the *in-situ* TEM measurements is schematically shown in Fig. 1a. A dedicated scanning transmission microscopy (STM)-TEM holder is used which uses piezo-electric scanners to controllably bring a metallic STM tip and the nano-pillar RRAM device in physical contact for electrical stressing and the electrical stimulus is provided using a ramp voltage stress (RVS). A current compliance is always used during electrical stress to limit the maximum current that can flow through the device and prevent unintentional hard breakdown. We employ TEM imaging to observe the real-time morphological and structural changes in the RRAM device in response to the electrical stimulus. These electrically stressed devices are then analyzed using scanning TEM (STEM) and X-ray energy dispersive spectroscopy (EDS) for physical and chemical analysis, respectively.

3.2. *In-situ TEM: Physical, chemical and electrical characterization*

Prior to *in-situ* TEM electrical stressing, we carried out a thorough physical and chemical analysis on the as-prepared devices which act as control samples to compare with the electrically stressed devices. A representative high angle annular dark field (HAADF) TEM micrograph of one of the nano-pillars acquired in STEM mode is shown in Fig. 2a. The contrast in the HAADF image is primarily governed by the electron scattering cross-sectional area [49]. As a rule of thumb, higher the atomic mass of an element, higher the scattering cross sectional area which leads to more electron scattering events. Therefore, a heavier element appears bright in the HAADF TEM micrograph. EDS maps of all the elements (including W, Hf, O, and Al) are shown in Fig. 2b-e. The elemental distribution within dielectric and metallic electrode layers is consistent with the device fabrication process flow.

A few interesting insights can be obtained for the oxygen elemental profile from the EDS map as shown in Fig. 2d. The presence of elemental oxygen is also found inside the bulk of W electrode which suggest the out-diffusion of oxygen from HfO_2 towards W electrode. However, no such significant redistribution of oxygen is found at the Al/Al_2O_3 interface. This confirms that W can act as oxygen (O^{2-}) reservoir and hence forms a scavenging layer in memristive devices. We would like to point out that, in an ideal case, W has very low reactivity towards oxygen. However, the deposition process and conditions could readily modify the material properties, including density, crystallinity, rugosity and grain boundary distribution, in the W films [50] which change its oxygen solubility and hence affects the RRAM performance [51]. The oxidation mechanism of W should be further studied and clarified in future works. The out-diffusion of oxygen ions leads to creation of a vacancy defect-rich HfO_2 layer at the W/HfO_2 interface (also known as buffer layer) assisting in the movement of oxygen ions during resistive switching. Unintentionally, this buffer layer has high interfacial defect density which results in a higher leakage current as will be shown latter during the *in-situ* electrical measurements. EDS line profile of all the elements across the vertical arrow shown in Fig. 2a is plotted in Fig. 2f. We find the presence of Al in HfO_2 and W layers, however no such diffusion of Hf and W is observed in the Al layer. The atomic radius and elemental mass of Al is much lower compared to both Hf and W and this increases its effective atomic/ion mobility and thereby increasing its

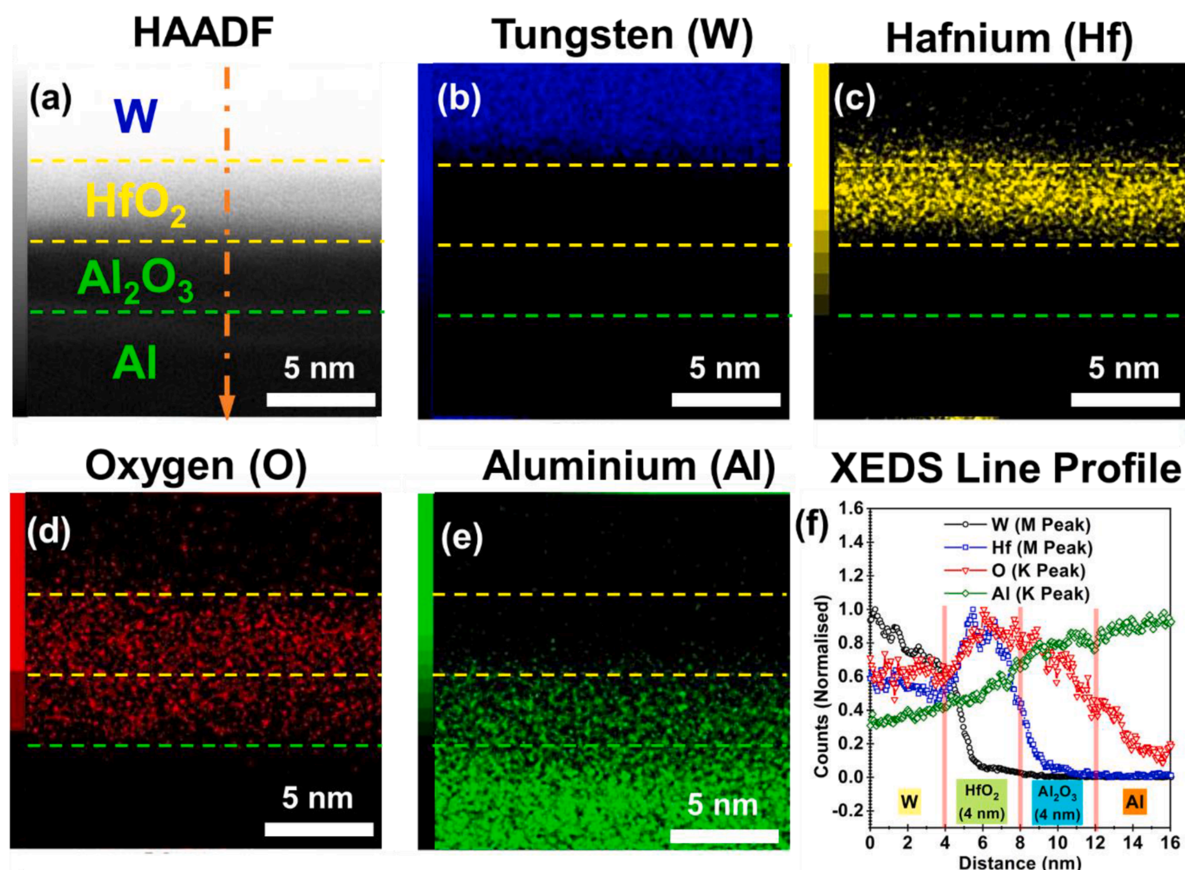

Fig. 2. a) High angle annular dark field (HAADF) scanning TEM (STEM) micrograph of one of the RRAM devices. b) - e) Elemental analysis of the switching oxides Al_2O_3 and HfO_2 and electrode layers (i.e., W and Al) is performed using X-ray energy dispersive spectroscopy (EDS). f) EDS line profiles along the vertical direction marked by arrow in (a) showing the relative distributions of O, Al, Hf and W in the oxide layers and metal electrodes. Each of the EDS line profiles shown in (f) has been normalised (to its maximum counts) to obtain the relative distribution.

diffusion in the adjacent material layers.

We first discuss the results of the negative polarity stress measurements as shown in Fig. 3. The device is subjected to current-compliance limited RVS cycles and the compliance is successively increased in steps from 1 μA to 2 mA as shown in Fig. 3a. The low bias *I-V* characteristics are extracted and plotted in Fig. 3b. The results show that the conductance increases progressively with successive RVS cycles mimicking the gradual conductance change in a memristor device.

We also track the real-time structural changes in the device during the *in-situ* electrical stressing by capturing the image frames at the rate of ~20 frames per second. The temporal snapshots of the device subjected to the negative RVS cycles are shown in Fig. 3c-f. Snapshots from the successive RVS cycling are chosen to show the growth of the defect. During the electrical stress, we observe the formation and evolution of nanoscale physical defects at the oxide interface as shown by the enclosed square regions in Fig. 3f. A HRTEM micrograph of the physical defect (highlighted by green color in Fig. 3f) region is shown in Fig. 4a where crystallization of both HfO_2 and Al_2O_3 oxide layers can be observed.

HRTEM micrograph of the same device from another area after electrical stress is shown in Fig. 4b. Both Al_2O_3 and HfO_2 layers show periodic fringes in the HRTEM micrographs, and these appear only after electrical stressing. Note that prior to any electrical stressing, the periodic fringes are absent in HRTEM micrographs as shown in Fig. 1c. This is because Al_2O_3 and HfO_2 layers are amorphous and polycrystalline respectively. These periodic fringes in the HRTEM micrographs, after electrical stressing, are indicative of the crystallization of both oxide layers. To understand it further, we extracted the intensity line profiles of HRTEM micrograph from Al, Al_2O_3, HfO_2 and W regions (as marked by solid arrows in Fig. 4b) and the results are plotted in Fig. 4c.

The solid arrows in the oxide and electrode regions are drawn over a distance of 4 nm and are perpendicular to the direction of Al (111) so as to compare the periodicity of lattice fringes in various material layers with Al. We find that the periodicity of the lattice fringes observed for Al_2O_3 and HfO_2 is identical and closely matches with that of the crystal plane of Al (111) [48]. This suggests the electron wind induced migration of Al towards oxides and W electrode, i.e., electromigration of Al due to the momentum exchange between injected electrons and Al ions. The maximum current density during negative polarity stress in the RRAM nano-device is of the same order of magnitude as typically observed for Al electromigration in CMOS interconnects [52–54] (see Supplementary Figure 2 for calculations).

The results of positive polarity electrical stressing is shown in Supplementary Figure 3. A fresh nano-pillar device is subjected to an RVS with a current compliance of ~1 μA. The current compliance is chosen carefully so as not to induce hard dielectric breakdown. A sharp jump in the current can be clearly observed at $V = 1.6$ V as shown in Supplementary Figure 3a. This is similar to soft breakdown typically observed in ultra-thin gate oxide films. The induced structural change in device is monitored in real-time by continuously capturing the corresponding TEM micrograph frames. The temporal TEM micrographs of the device for the three regions (S1, S2 and S3) highlighted in Supplementary Figure 3a are shown in Supplementary Figures 3b-d. We observe the formation of nanoscale physical defect at the interface between HfO_2 and Al_2O_3 layers as shown in Supplementary Figure 3b in stage S1. The defect grows during subsequent electrical stressing and finally appears as an extended line defect at the interface between the oxide layers at the end of stage S3. This is an interesting observation suggesting that the

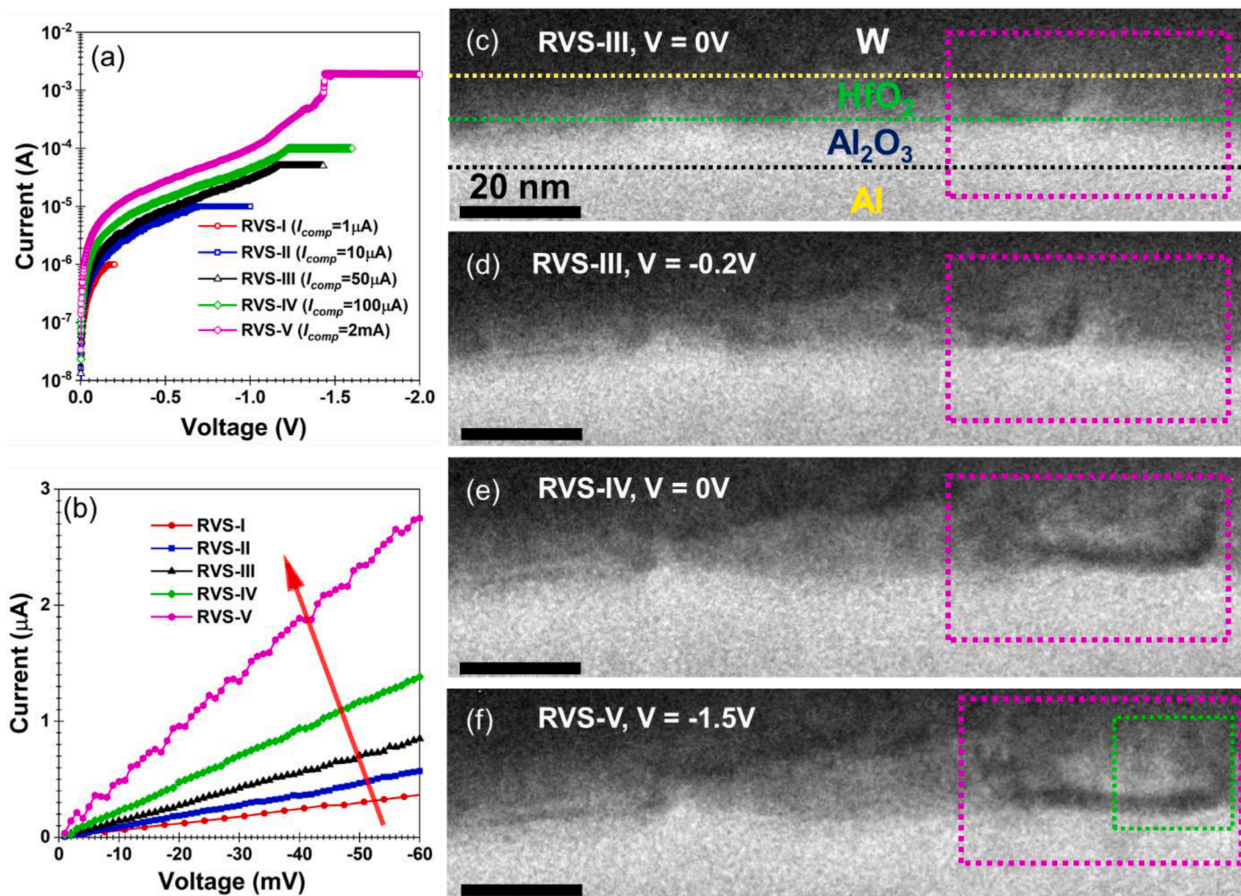

Fig. 3. a) *I-V* characteristics of a RRAM device under negative ramp voltage stress (RVS). The current compliance is gradually increased from 1 μA to 2 mA during successive RVS stressing. b) *I-V* plot showing the gradual increase in conductivity with successive RVS cycles. c-f) Temporal snapshots of the RRAM device during the electrical stress showing the growth and evolution of physical defects at Al_2O_3 and HfO_2 interface.

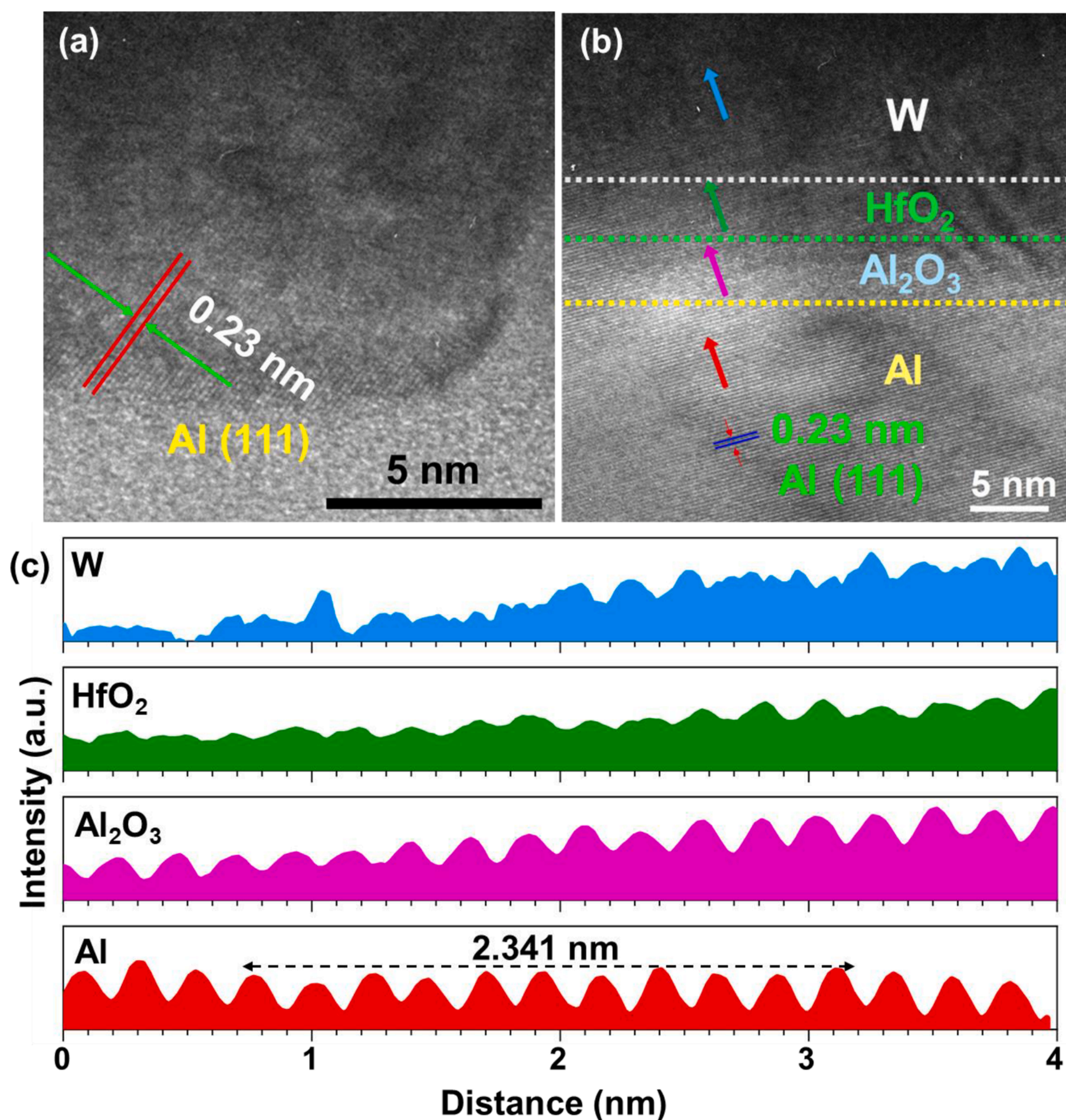

Fig. 4. a) A HRTEM imaging is performed at the interfacial region outlined in Fig. 3(f) (in green box) showing crystallization after electrical stress. b) The HRTEM micrograph of another such area of the device showing significant crystallization of Al_2O_3 and HfO_2. c) The intensity line profile of the HRTEM micrograph for Al, Al_2O_3, HfO_2 and W at the locations shown by solid arrow symbols in (b) is plotted. The solid arrows are drawn over a distance of 4 nm and are perpendicular to the direction of Al (111). Analysis shows that periodicity of the observed lattice fringes is ~0.23 nm which closely matches with that of Al (111).

Al_2O_3/HfO_2 interface plays a crucial role in the switching process and soft dielectric breakdown in the bilayer oxide stacks. These findings are consistent with our prior *in-situ* TEM observations of interfacial defects observed after a soft breakdown in Al_2O_3/ZrO_2 bilayer dielectric stacks [55].

Bipolar switching is attempted on a fresh device to understand the physical origins of the switching mechanism. One such switching data is presented in Fig. 5 where a threshold switching [56] is observed for both the electrical polarities. We first apply a positive polarity RVS ($I_{comp} = 2$ mA) to bring the device to the low resistance state (LRS). Then, the voltage is slowly ramped down, and the device itself recovers its high resistance state (HRS) at 0.2 V. Similarly, an RVS is applied with negative polarity ($I_{comp} = 2$ mA) brings the device to LRS, although with a lower set voltage than that of the first positive cycle. A real-time video is also captured during the bipolar switching and is shown in Supplementary Movie 1 where migration of Al can be observed. HRTEM analysis was carried out on the device after bipolar switching and the results are shown in Fig. 5b. We observe the presence of crystallization in both HfO_2 and Al_2O_3 as also seen previously in Fig. 4a,b. Further analysis shows that the periodicity of the observed lattice fringes is ~0.23 nm which closely matches to that of Al (111) [48]. This suggests that Al plays a dominant role in the switching mechanism of $W/HfO_2/Al_2O_3/Al$-based RRAM devices.

Finally, we use STEM and EDS to study the chemical origin of the switching process. We provide a thorough investigation of all the elements including Hf, Al, O and W for both positive and negative polarity stressed devices. These results are also compared with the control/unstressed devices as shown in Fig. 6. We first use STEM to identify the

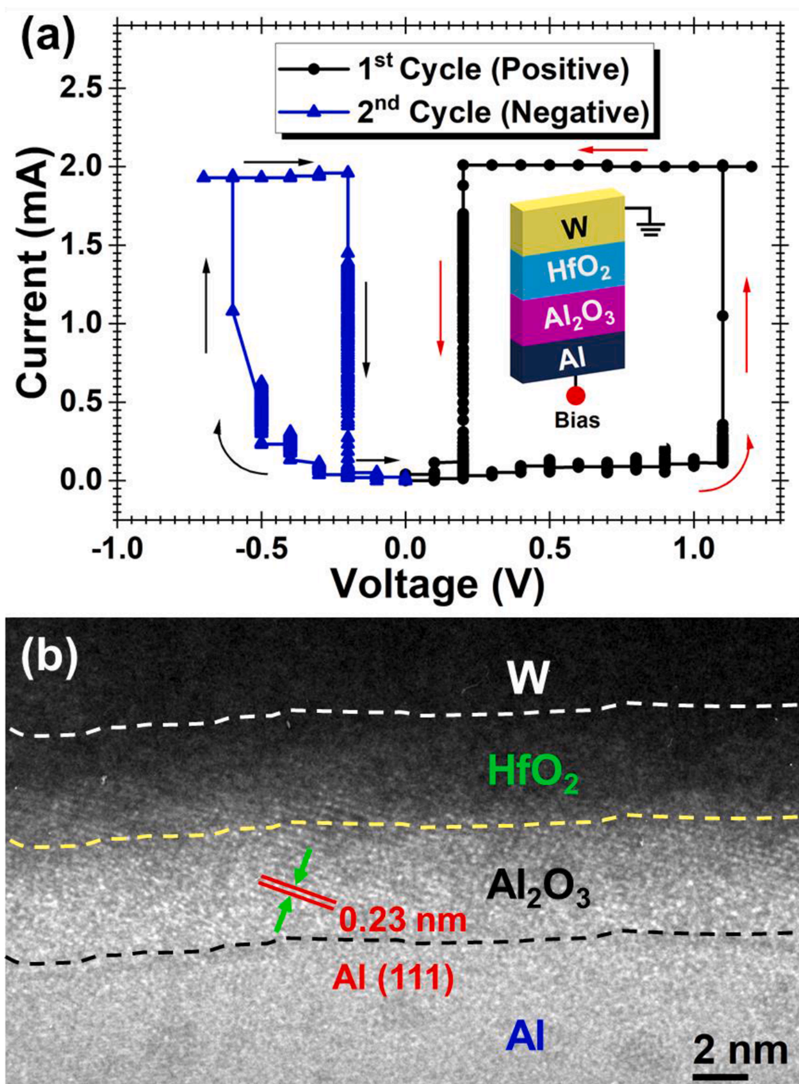

Fig. 5. a) *In-situ I-V* characteristics of a RRAM device showing threshold resistive switching in both polarities. While the first SET voltage (i.e., electroforming voltage) requires ~1 V, the SET voltage is significantly reduced (by ~0.5 V) for subsequent cycle when switching is performed with negative polarity. b) A HRTEM micrograph of a device which has undergone a full positive and a negative switching cycle shows prominent crystallization in both HfO_2 and Al_2O_3 switching oxide layers. The periodicity of the lattice fringes matches with that of Al (see Fig. 1c) suggesting a dominant role of Al in the resistive switching process.

potential region of interest where morphological/structured changes are observed during the electrical stressing (see Fig. 4) and EDS analysis carried out on these identified areas to map their chemical composition. While a small migration of W and Hf is observed for either of the stress polarities, we clearly observe the massive redistribution of O and Al after electrical stress. Notable is the migration of Al in the bulk oxides (and also in the W top electrode) which is observed consistently for both the electrical polarities. When Al is at positive potential, Al changes from its atomic state to its ionic state, Al^{3+}, and its migration/diffusion in the oxide bulk is predominantly due to applied electric field. This is unlike the case at negative polarity, where Al migrates into the oxide due to electron wind forces or electromigration [52–54]. Furthermore, by comparing the Al intensity inside W layer in the "negative" and "positive" electrical bias, we infer that the effect of electromigration is stronger than ionic diffusion possibly due to its lower barrier and activation energy. Oxygen gets redistributed in the oxide layers as well as the metal electrodes and no preferential effect of electrical polarity is observed. This is likely as Al acts as dominant active species for resistive switching at high current densities and therefore no preferential redistribution of oxygen ions is observed in this case.

Based on the detailed *in-situ* electrical, physical, and chemical analysis, we suggest that diffusion barriers between Al and switching dielectric layers must be preferentially included to improve the switching performance and overall reliability of RRAM devices for cases where Al is used as an active electrode. The use of Al_2O_3 as diffusion barrier for oxygen ions should be considered given it can be also potentially used as a barrier between W/HfO_2 interface preventing further oxygen scavenging by the defects within W layer. For future experiments, we also recommend using electron energy loss spectroscopy (EELS) for identifying the chemical nature of Al and oxygen elements distributed in the MIM structure before and after positive/negative stressing of the same sample. This could provide further evidence on how application of a potential or bias to the Al electrode changes its atomic state to its ionic state (Al^{3+}) and directly probe the migration of this Al^{3+} species in the oxide bulk under electric field.

4. Conclusions

In this study, we have used *in-situ* transmission electron microscopy (TEM) and X-ray energy dispersive spectroscopy (EDS) to investigate the switching mechanism in HfO_2 and Al_2O_3 bilayer resistive random access memory (RRAM) devices. EDS analysis suggests the existence of two competing physical mechanisms including the redistribution of oxygen ions and the migration of Al species in the resistive switching process. We observe that the use of Al as an active electrode causes severe migration of Al species in the bulk of the bilayered oxides, leading to the device to fail to reset. This study suggests the choice of active electrode in HfO_2/Al_2O_3 bilayer RRAM stack is an important consideration in its

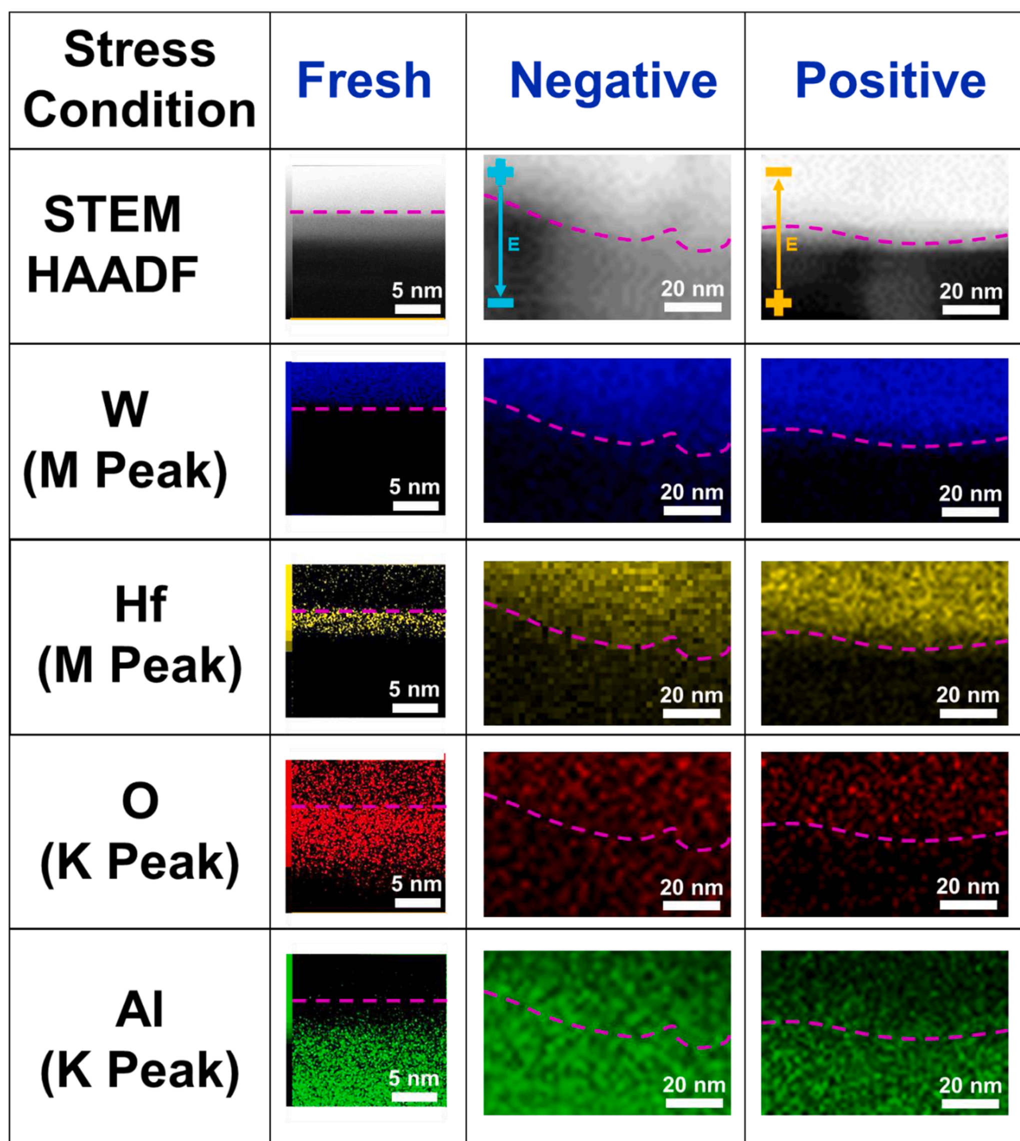

Fig. 6. EDS elemental distributions of W, Hf, O and Al in W/HfO_2/Al_2O_3/Al under various electrical stress conditions. The STEM micrograph and the elemental distributions for fresh/unstressed, negatively stressed and positively stressed devices are shown side-by-side for comparisons. The dotted line (in pink color) represents the W-HfO_2 interface. For the as prepared devices, W acts as oxygen scavenging layer and therefore a significant count of oxygen is present in W layer. For both positively and negatively stressed devices, we observe a dominant aluminum migration and oxygen redistribution in both HfO_2 and Al_2O_3 layers and W electrode.

overall switching performance and reliability.

CRediT authorship contribution statement

Alok Ranjan: Conceptualization, Methodology, Formal analysis, Writing – original draft, Visualization, Writing – review & editing. **Hejun Xu:** Methodology, Formal analysis, Visualization. **Chaolun Wang:** Methodology, Formal analysis. **Joel Molina:** Methodology, Formal analysis. **Xing Wu:** Supervision, Project administration, Funding acquisition, Writing – review & editing. **Hui Zhang:** Project administration. **Litao Sun:** Project administration, Funding acquisition. **Junhao Chu:** Project administration, Funding acquisition. **Kin Leong Pey:** Conceptualization, Supervision, Project administration, Funding acquisition, Writing – review & editing.

Declaration of Competing Interest

The authors declare that they have no known competing financial interests or personal relationships that could have appeared to influence the work reported in this paper.

Data availability

Data will be made available on request.

Acknowledgements

The work is primarily funded by Kwan Im Thong Hood Cho Temple Chair Professorship grant at Singapore University of Technology and Design (SUTD). Support from other research grants including Projects of Science and Technology Commission of Shanghai Municipality Grant Nos. (19ZR1473800, 14DZ2260800), the Shanghai Rising-Star Program (17QA1401400), Young Elite Scientists Sponsorship Program by CAST (YESS) and Fundamental Research Funds for the Central Universities are also acknowledged.

Supplementary materials

Supplementary material associated with this article can be found, in the online version, at doi:10.1016/j.apmt.2023.101739.

References

[1] A. Chen, A review of emerging non-volatile memory (NVM) technologies and applications, Solid State Electron. 125 (2016) 25–38, https://doi.org/10.1016/j.sse.2016.07.006.

[2] E. Carlos, R. Branquinho, R. Martins, A. Kiazadeh, E. Fortunato, Recent progress in solution-based metal oxide resistive switching devices, Adv. Mater. 33 (2021), 2004328, https://doi.org/10.1002/adma.202004328.

[3] E. Carlos, A. Kiazadeh, J. Deuermeier, R. Branquinho, R. Martins, E. Fortunato, Critical role of a double-layer configuration in solution-based unipolar resistive switching memories, Nanotechnology 29 (2018), 345206, https://doi.org/10.1088/1361-6528/aac9fb.

[4] M.E. Pereira, J. Deuermeier, P. Freitas, P. Barquinha, W. Zhang, R. Martins, E. Fortunato, A. Kiazadeh, Tailoring the synaptic properties of a-IGZO memristors for artificial deep neural networks, APL Mater. 10 (2022), 011113, https://doi.org/10.1063/5.0073056.

[5] S. Menzel, M. von Witzleben, V. Havel, U. Böttger, The ultimate switching speed limit of redox-based resistive switching devices, Faraday Discuss. 213 (2019) 197–213, https://doi.org/10.1039/C8FD00117K.

[6] M. von Witzleben, T. Hennen, A. Kindsmüller, S. Menzel, R. Waser, U. Böttger, Study of the SET switching event of VCM-based memories on a picosecond timescale, J. Appl. Phys. 127 (2020), 204501, https://doi.org/10.1063/5.0003840.

[7] U. Böttger, M. von Witzleben, V. Havel, K. Fleck, V. Rana, R. Waser, S. Menzel, Picosecond multilevel resistive switching in tantalum oxide thin films, Sci. Rep. 10 (2020) 16391, https://doi.org/10.1038/s41598-020-73254-2.

[8] C.H. Cheng, A. Chin, F.S. Yeh, Ultralow switching energy Ni/GeOx/HfON/TaN RRAM, IEEE Electron Device Lett. 32 (2011) 366–368, https://doi.org/10.1109/LED.2010.2095820.

[9] C.H. Cheng, C.Y. Tsai, A. Chin, F.S. Yeh, High performance ultra-low energy RRAM with good retention and endurance, in: 2010 International Electron Devices Meeting, 2010, https://doi.org/10.1109/IEDM.2010.5703392.

[10] A. Ranjan, N. Raghavan, J. Molina, S.J. O'Shea, K. Shubhakar, K.L. Pey, Analysis of quantum conductance, read disturb and switching statistics in HfO2 RRAM using conductive AFM, Microelectron. Reliab. 64 (2016) 172–178, https://doi.org/10.1016/j.microrel.2016.07.112.

[11] B. Govoreanu, G.S. Kar, Y. Chen, V. Paraschiv, S. Kubicek, A. Fantini, et al., 10×10nm2 Hf/HfOx crossbar resistive RAM with excellent performance, reliability and low-energy operation, in: 2011 International Electron Devices Meeting, 2011, https://doi.org/10.1109/IEDM.2011.6131652.

[12] W. Song, W. Wang, H.K. Lee, M. Li, V.Y.-Q. Zhuo, Z. Chen, et al., Analog switching characteristics in TiW/Al2O3/Ta2O5/Ta RRAM devices, Appl. Phys. Lett. 115 (2019), 133501, https://doi.org/10.1063/1.5100075.

[13] Y. Sun, H. Xu, C. Wang, B. Song, H. Liu, Q. Liu, S. Liu, Q. Li, A Ti/AlOx/TaOx/Pt analog synapse for memristive neural network, IEEE Electron Device Lett. 39 (2018) 1298–1301, https://doi.org/10.1109/LED.2018.2860053.

[14] S. Stathopoulos, A. Khiat, M. Trapatseli, S. Cortese, A. Serb, I. Valov, T. Prodromakis, Multibit memory operation of metal-oxide bi-layer memristors, Sci. Rep. 7 (2017) 17532, https://doi.org/10.1038/s41598-017-17785-1.

[15] S. Yin, Y. Kim, X. Han, H. Barnaby, S. Yu, Y. Luo, W. He, X. Sun, J. Kim, J. Seo, Monolithically integrated RRAM- and CMOS-based in-memory computing optimizations for efficient deep learning, IEEE Micro 39 (2019) 54–63, https://doi.org/10.1109/MM.2019.2943047.

[16] A. Valentian, F. Rummens, E. Vianello, T. Mesquida, C.L. d. Boissac, O. Bichler, and C. Reita, "Fully integrated spiking neural network with analog neurons and RRAM synapses", *2019 IEEE International Electron Devices Meeting (IEDM)*, (2019). 10.1109/IEDM19573.2019.8993431.

[17] H.P. Wong, H. Lee, S. Yu, Y. Chen, Y. Wu, P. Chen, B. Lee, F.T. Chen, M. Tsai, Metal–Oxide RRAM", Proc. IEEE 100 (2012) 1951–1970, https://doi.org/10.1109/JPROC.2012.2190369.

[18] R. Waser, R. Dittmann, G. Staikov, K. Szot, Redox-based resistive switching memories - Nanoionic mechanisms, prospects, and challenges, Adv. Mater. 21 (2009) 2632–2663, https://doi.org/10.1002/adma.200900375.

[19] E.A. Cartier, W. Kim, N. Gong, T. Gokmen, M.M. Frank, D.M. Bishop, et al., Reliability challenges with materials for analog computing, in: 2019 IEEE International Reliability Physics Symposium (IRPS), 2019, https://doi.org/10.1109/IRPS.2019.8720599.

[20] J. del Valle, J.G. Ramírez, M.J. Rozenberg, I.K. Schuller, Challenges in materials and devices for resistive-switching-based neuromorphic computing, J. Appl. Phys. 124 (2018), 211101, https://doi.org/10.1063/1.5047800.

[21] N. Raghavan, R. Degraeve, L. Goux, A. Fantini, D.J. Wouters, G. Groeseneken, M. Jurczak, RTN insight to filamentary instability and disturb immunity in ultra-low power switching HfOx and AlOx RRAM, 2013, Sympos. VLSI Technol. (2013).

[22] A. Ranjan, N. Raghavan, K. Shubhakar, S.J. O'Shea, K.L. Pey, "Random telegraph noise nano-spectroscopy in high-κ dielectrics using scanning probe microscopy techniques,". Noise in Nanoscale Semiconductor Devices, Springer International Publishing, 2020, pp. 417–440.

[23] G. Hilson, Weebit, CEA-Leti advance ReRAM technology. EE-Times, ed, 2022.

[24] H.Y. Lee, P.S. Chen, T.Y. Wu, Y.S. Chen, C.C. Wang, P.J. Tzeng, C.H. Lin, F. Chen, C.H. Lien, M. Tsai, Low power and high speed bipolar switching with a thin reactive Ti buffer layer in robust HfO2 based RRAM, in: 2008 IEEE International Electron Devices Meeting, 2008, https://doi.org/10.1109/IEDM.2008.4796677.

[25] Y.Y. Chen, R. Degraeve, S. Clima, B. Govoreanu, L. Goux, A. Fantini, Understanding of the endurance Failure in Scaled HfO2-based 1T1R RRAM through vacancy mobility degradation, in: 2012 IEEE International Electron Devices Meeting, 2012, https://doi.org/10.1109/IEDM.2012.6479079.

[26] Y.Y. Chen, B. Govoreanu, L. Goux, R. Degraeve, A. Fantini, G.S. Kar, et al., Balancing SET/RESET Pulse for >10(10) Endurance in HfO2/Hf 1T1R Bipolar RRAM, IEEE Trans. Electron. Dev. 59 (2012) 3243–3249, https://doi.org/10.1109/ted.2012.2218607.

[27] M.M. Mallol, M.B. Gonzalez, F. Campabadal, Impact of the HfO2/Al2O3 stacking order on unipolar RRAM devices, Microelectron. Eng. 178 (2017) 168–172, https://doi.org/10.1016/j.mee.2017.05.024.

[28] F. Yuan, S. Shen, Z. Zhang, L. Pan, J. Xu, Interface-induced two-step RESET for filament-based multi-level resistive memory, Superlattices Microstruct. 91 (2016) 90–97, https://doi.org/10.1016/j.spmi.2015.12.044.

[29] X. Huang, H. Wu, G. Bin, D.C. Sekar, L. Dai, M. Kellam, G. Bronner, N. Deng, H. Qian, HfO2/Al2O3multilayer for RRAM arrays: a technique to improve tail-bit retention, Nanotechnology 27 (2016), 395201, https://doi.org/10.1088/0957-4484/27/39/395201.

[30] K. Wan Gee, K. Ja Yong, M. Ji Won, J. Moon Sig, C. Hye Jung, K. Soo Gil, L. Kee Jeung, H. Kwon, P. Sung Ki, Effect of Inserting Al2O3 layer and device structure in HfO2-Based ReRAM for low power operation, in: 2012 4th IEEE International Memory Workshop, 2012, https://doi.org/10.1109/IMW.2012.6213681.

[31] C.Y. Huang, J.H. Jieng, W.Y. Jang, C.H. Lin, T.Y. Tseng, Improved resistive switching characteristics by Al2O3 layers inclusion in HfO2-Based RRAM devices, ECS Solid State Lett. 2 (2013) P63–P65, https://doi.org/10.1149/2.006308ssl.

[32] S. Park, K. Cho, J. Jung, S. Kim, Annealing effect of Al2O3 tunnel barriers in HfO2-Based ReRAM DEVICES on nonlinear resistive switching characteristics, J. Nanosci. Nanotechnol. 15 (2015) 7569–7572, https://doi.org/10.1166/jnn.2015.11138.

[33] L.-.G. Wang, X. Qian, Y.-.Q. Cao, Z.-.Y. Cao, G.-.Y. Fang, A.-.D. Li, D. Wu, Excellent resistive switching properties of atomic layer-deposited Al2O3/HfO2/Al2O3 trilayer structures for non-volatile memory applications, Nanoscale Res. Lett. 10 (2015) 135, https://doi.org/10.1186/s11671-015-0846-y.

[34] M. Trapatseli, S. Cortese, A. Serb, A. Khiat, T. Prodromakis, Impact of ultra-thin Al2O3–y layers on TiO2–x ReRAM switching characteristics", J. Appl. Phys. 121 (2017), 184505 https://doi.org/10.1063/1.4983006.

[35] E. Shahrabi, C. Giovinazzo, J. Sandrini, Y. Leblebici, The key impact of incorporated Al2O3 barrier layer on W-based ReRAM switching performance, in: 2018 14th Conference on Ph.D. Research in Microelectronics and Electronics (PRIME), 2018, https://doi.org/10.1109/PRIME.2018.8430371.

[36] C. Mahata, S. Kim, Multi-level resistive switching in HfO2/Al2O3/HfO2 based memristor on transparent ITO electrode, in: 2020 International Conference on Electronics, Information, and Communication (ICEIC), 2020, https://doi.org/10.1109/ICEIC49074.2020.9051025.

[37] X. Li, C.H. Tung, K.L. Pey, The nature of dielectric breakdown, Appl. Phys. Lett. 93 (2008), https://doi.org/10.1063/1.2974792.

[38] X. Li, C.H. Tung, K.L. Pey, The radial distribution of defects in a percolation path, Appl. Phys. Lett. 93 (2008), https://doi.org/10.1063/1.3056659.

[39] C. Li, B. Gao, Y. Yao, X. Guan, X. Shen, Y. Wang, et al., Direct observations of nanofilament evolution in switching processes in HfO2-based resistive random access memory by In Situ TEM studies, Adv. Mater. 29 (2017), 1602976, https://doi.org/10.1002/adma.201602976.

[40] J. Kwon, Y.N. Picard, M. Skowronski, A.A. Sharma, J.A. Bain, Situ biasing TEM investigation of resistive switching events in TiO2-based RRAM, in: 2014 IEEE International Reliability Physics Symposium, 2014, https://doi.org/10.1109/IRPS.2014.6860680.

[41] G.-.S. Park, Y.B. Kim, S.Y. Park, X.S. Li, S. Heo, M.-.J. Lee, et al., In situ observation of filamentary conducting channels in an asymmetric Ta2O5−x/TaO2−x bilayer structure, Nat. Commun. 4 (2013) 2382, https://doi.org/10.1038/ncomms3382.

[42] S. Mei, M. Bosman, R. Nagarajan, X. Wu, K.L. Pey, Compliance current dominates evolution of NiSi2 defect size in Ni/dielectric/Si RRAM devices, Microelectron. Reliab. 61 (2016) 71–77, https://doi.org/10.1016/j.microrel.2015.12.037.

[43] X. Wu, S. Mei, M. Bosman, N. Raghavan, X. Zhang, D. Cha, K. Li, K.L. Pey, Evolution of filament formation in Ni/HfO2/SiOx/Si-Based RRAM Devices, Adv. Electron. Mater. 1 (2015), 1500130, https://doi.org/10.1002/aelm.201500130.

[44] X. Wu, K. Li, N. Raghavan, M. Bosman, Q.-.X. Wang, D. Cha, X.-.X. Zhang, K.-.L. Pey, Uncorrelated multiple conductive filament nucleation and rupture in ultra-thin high-κ dielectric based resistive random access memory, Appl. Phys. Lett. 99 (2011), 093502, https://doi.org/10.1063/1.3624597.

[45] K. Baek, S. Park, J. Park, Y.-.M. Kim, H. Hwang, S.H. Oh, In situ TEM observation on the interface-type resistive switching by electrochemical redox reactions at a TiN/PCMO interface, Nanoscale 9 (2017) 582–593, https://doi.org/10.1039/C6NR06293H.

[46] K.B. Jinesh, Y. Lamy, R.A.M. Wolters, J.H. Klootwijk, E. Tois, F. Roozeboom, W.F. A. Besling, Silicon out-diffusion and aluminum in-diffusion in devices with atomic-layer deposited La2O3 thin films, Appl. Phys. Lett. 93 (2008), 192912, https://doi.org/10.1063/1.3025850.

[47] M. Qi, C. Guo, M. Zeng, Oxygen vacancy kinetics mechanism of the negative forming-free process and multilevel resistance based on hafnium oxide RRAM, J. Nanomater. 2019 (2019), 6724018, https://doi.org/10.1155/2019/6724018.

[48] B.F. Figgins, G.O. Jones, D.P. Riley, LXXVII. The thermal expansion of aluminium at low temperatures as measured by an X-ray diffraction method, Philos. Mag. 1 (1956) 747–758, https://doi.org/10.1080/14786435608238150.

[49] D.B. Williams, C.B. Carter, Transmission Electron Microscopy, 2 ed., Springer US, 2009.

[50] C. Ren, Z.Z. Fang, M. Koopman, B. Butler, J. Paramore, S. Middlemas, Methods for improving ductility of tungsten - a review, Int. J. Refractory Metals Hard Mater. 75 (2018) 170–183, https://doi.org/10.1016/j.ijrmhm.2018.04.012.

[51] E. Shahrabi, ReRAM from material study to CMOS Co-integration. PhD, Microsystems and Microelectronics, Ecole Polytechnique Fédérale De Lausanne, 2019.

[52] Temperature-dependent Electromigration Reliability, Electrothermal Analysis of VLSI Systems, Springer US, 2002, pp. 121–155.

[53] R.E. Hummel, Electromigration and related failure mechanisms in integrated circuit interconnects, Int. Mater. Rev. 39 (1994) 97–112, https://doi.org/10.1179/imr.1994.39.3.97.

[54] J.R. Black, Electromigration failure modes in aluminum metallization for semiconductor devices, Proc. IEEE 57 (1969) 1587–1594, https://doi.org/10.1109/PROC.1969.7340.

[55] X. Wu, C. Luo, P. Hao, T. Sun, R.S. Wang, C.L. Wang, et al., Probing and manipulating the interfacial defects of InGaAs dual-layer metal oxides at the atomic scale, Adv. Mater. 30 (2018), https://doi.org/10.1002/adma.201703025.

[56] S. Menzel, U. Böttger, M. Wimmer, M. Salinga, Physics of the switching kinetics in resistive memories, Adv. Funct. Mater. 25 (2015) 6306–6325, https://doi.org/10.1002/adfm.201500825.